Shell model potential for $PbTiO_3$ and its applicability to surfaces and domain walls

2008 J. Phys.: Condens. Matter 20 325225

(http://iopscience.iop.org/0953-8984/20/32/325225)

J. Phys.: Condens. Matter **20** (2008) 325225 (11pp) doi:10.1088/0953-8984/20/32/325225

Shell model potential for $PbTiO_3$ and its applicability to surfaces and domain walls

T Shimada[1], K Wakahara[2], Y Umeno[3] and T Kitamura[1]

[1] Department of Mechanical Engineering and Science, Graduate School of Engineering, Kyoto University, Yoshida-hommachi, Sakyo-ku, Kyoto 606-8501, Japan
[2] Matsushita Electric Works, Ltd, 1048, Kadoma, Kadoma-shi, Osaka 571-8686, Japan
[3] Department of Fundamental Engineering, Institute of Industrial Science, The University of Tokyo, 4-6-1 Komaba Meguro-ku, Tokyo 153-8505, Japan

E-mail: shimada@cyber.kues.kyoto-u.ac.jp

Received 11 April 2008, in final form 23 June 2008
Published 18 July 2008
Online at stacks.iop.org/JPhysCM/20/325225

Abstract

We have developed an efficient interatomic potential for $PbTiO_3$ in the framework of the shell model by fitting its parameters to reproduce both the mechanical and ferroelectric properties derived from *ab initio* density functional theory calculations. The optimized potential successfully yields the crystal structures, elastic properties and phonon dispersion curves, whereas the spontaneous polarization and effective charges are slightly underestimated. It reproduces well characteristic ferroelectric (FE) and antiferrodistortive (AFD) instabilities closely associated with the structural phase transition in $PbTiO_3$, and is reliable under high tension and compression along the [001] direction. Furthermore, the potential is effective enough to describe 180° and 90° domain walls as well as the PbO-terminated surface with c(2 × 2) reconstruction where the FE and AFD distortions coexist. This significant success widely extends the applicable range of atomic-level simulations of ferroelectrics based on the shell model potential.

1. Introduction

Lead titanate ($PbTiO_3$) and its solid solutions, such as $Pb(Zr, Ti)O_3$ (PZT) and $Pb(Mg_{1/3}, Nb_{2/3})O_3$-$PbTiO_3$ (PMN-PT), have attracted much attention owing to their outstanding electromechanical properties, and have been widely applied in technological devices including nonvolatile random access memories (FeRAMs), actuators and sensors [1–4]. Significant advances in manufacturing technology have enabled us to obtain nanostructured ferroelectric materials, e.g., ultrathin films [6, 7], nanowires (tubes) [8–10] and nanoislands [11, 12]. In such nanoscale materials, even a slight atomic displacement strongly affects both mechanical and ferroelectric properties, leading to critical malfunction of devices in some cases. Thus, design and reliability issues require an understanding of the atomic behavior of ferroelectrics. Computational simulation is a promising tool for the analysis of properties.

Ab initio (first-principles) calculations based on the density functional theory (DFT) [13, 14] have been extensively applied to ferroelectrics including $PbTiO_3$, and they have successfully provided a fundamental insight into the origin of ferroelectricity [5]. The studies have now been extended to properties in a body with surfaces [15–17], domain walls [18–20], grain boundaries [21–23], etc [24–26]. Although *ab initio* calculations are a rigorous and powerful tool, the heavy computational load imposes restrictions on the number of atoms and the temperature in a simulation system.

Atomic simulation [27] using an interatomic potential on the basis of the shell model [28] is one of the computationally efficient approaches for studying ferroelectrics. Ferroelectricity stems from the delicate balance between long-range Coulomb and short-range repulsive interactions, and the shell model can explicitly represent both. Moreover, the model is capable of describing ionic polarizability assuming two hypothetical particles, a core and a shell, which represent an atomic nucleus and electron shell, respectively. A shell model potential for $BaTiO_3$ developed by Tinte *et al* [29] based on *ab initio* calculations successfully reproduces not only the crystal structure, but also the temperature-dependent phase transition. This signifies that the model can reproduce the static and dynamic properties of ferroelectrics.

In the present study, we aim to develop an interatomic potential for $PbTiO_3$ in the framework of the shell model.

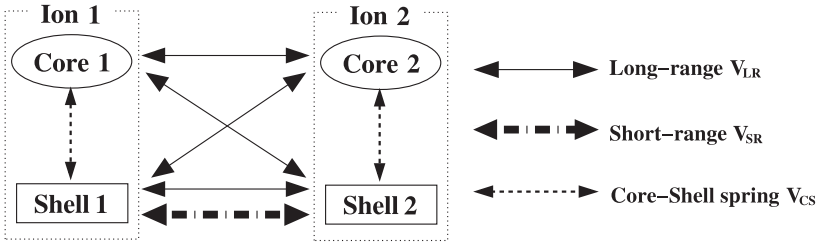

Figure 1. Schematic illustration of pair potential interactions between cores and shells in the framework of the shell model.

To this end, the parameters in the shell model functions are carefully fitted so that the potential correctly reproduces the fundamental properties of the single crystal, including crystal structures, elastic constants, effective charges and phonon dispersion relations derived from *ab initio* DFT calculations. After a desirable set of parameters is obtained, the reliability is examined by simulations under highly strained conditions. Furthermore, applicability to a body with surfaces and domain walls, where ferroelectricity is influenced by the structural discontinuity, is also investigated. In each part, we compare the available results of the potential for $PbTiO_3$ which was first derived by Sepliarsky *et al* [30] with those of our potential.

2. Optimization procedure of shell model potential

2.1. Shell model potential functions

In the framework of the shell model [28], an ion consists of two hypothetical particles, a core and a shell, which represent the atomic nucleus and electron shell, respectively. The core has a charge of X and a mass of the ion, whereas the shell has a charge of Y and no mass. The sum of X and Y gives the charge of the ion, Z. The displacement between the core and shell accounts for the electronic polarizability. Hence, the polarization in the $\alpha(= x, y, z)$ direction, P_α, is evaluated by the equation [31],

$$P_\alpha = \sum_\kappa (Z_\kappa \xi_{\kappa,\alpha} + Y_\kappa \zeta_{\kappa,\alpha}), \tag{1}$$

where $\xi_{\kappa,\alpha}$ and $\zeta_{\kappa,\alpha}$ denote the sublattice displacement of a core and the shell displacement with respect to the corresponding core of ion κ, respectively.

Figure 1 schematizes the interactions between the cores and shells of two ions. Three types of interactions, the long-range V_{LR}, short-range V_{SR} and core–shell spring V_{CS} potentials are defined in the shell model.

$$V_{LR}(r) = \frac{q_i q_j}{4\pi\varepsilon_0}\frac{1}{r}, \tag{2}$$

$$V_{SR}(r) = \left\{ A\exp\left(-\frac{r}{\rho}\right) - \frac{C}{r^6}\right\} f_c(r), \tag{3}$$

$$f_c(r) = \begin{cases} 1, & (r \leqslant R_{c1}) \\ \dfrac{1}{2}\cos\left(\dfrac{r - r_{c1}}{r_{c2} - r_{c1}}\pi\right) + \dfrac{1}{2}, & (R_{c1} < r \leqslant R_{c2}) \\ 0, & (R_{c2} < r) \end{cases} \tag{4}$$

$$V_{CS}(r) = \tfrac{1}{2}k_2 r^2 + \tfrac{1}{24}k_4 r^4, \tag{5}$$

where q, ε_0 and r denote the charge of the core or shell, the dielectric constant in vacuum and the distance between two particles, respectively. A, ρ, C, k_2, k_4 are parameters to characterize the pair interactions. The long-range potential represents the Coulomb interaction and the short-range potential shows the repulsive interaction. For the short-range potential, several functions are proposed [32]. In this study, we select the Buckingham potential which is often used in shell model studies. The short-range interaction is smoothly truncated thanks to the cut-off function $f_c(r)$ among the cut-off radii, R_{c1} and R_{c2}. Although the harmonic interaction was originally defined as the core–shell spring potential, we employ the nonlinear interaction including a fourth-order anharmonic term, which is effective for description of the hybridization effect on ionic polarizability in perovskite oxides [33].

The parameters required for $PbTiO_3$ can be summarized as follows: X, Y, k_2 and k_4 for all cores and shells of Pb, Ti and O, and A, ρ and C for all bonds between Pb–O, O–O, Ti–O and Pb–Ti. Note that the number of independent parameters is 23 because we impose a charge-neutrality constraint: the sum of the core and shell charges in the $PbTiO_3$ unit cell must be zero.

2.2. Derivation of physical properties of $PbTiO_3$ from ab initio calculations

The $PbTiO_3$ targeted in this study exhibits a single-phase transition from the paraelectric cubic phase to the ferroelectric tetragonal phase. The parameters in the shell model functions are fitted to fundamental properties of both the cubic and tetragonal $PbTiO_3$ single crystal, namely the equilibrium lattice constants, elastic constants, Born effective charges and phonon dispersion curves as well as the energy difference between the phases. These properties are accurately derived from *ab initio* (first-principles) DFT calculations using the PWSCF (Plane-Wave Self-Consistent Field) code [42]. Figure 2 shows the simulation models of the cubic and tetragonal $PbTiO_3$ used in the *ab initio* calculations as well as the potential optimization. The electronic wavefunctions are expanded in-plane waves up to a cut-off energy of 680 eV. We employ the Vanderbilt-type ultrasoft pseudopotentials (USPP) [34], which explicitly include the O 2s and 2p, the Ti 3s, 3p, 3d, and 4s, and the Pb 5d, 6s, and 6p electrons in the valence states. The ultrasoft pseudopotentials provided by the PWSCF were preliminarily validated by calculating the lattice

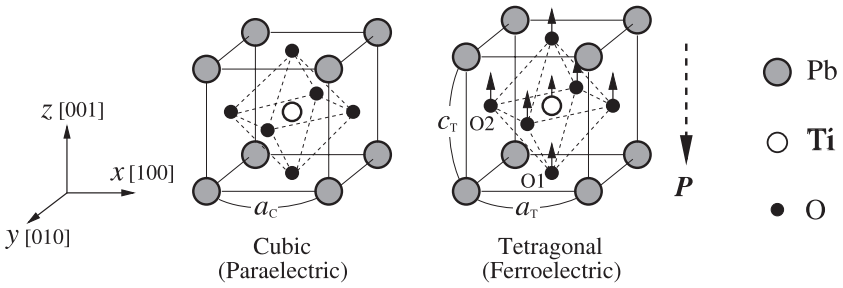

Figure 2. Simulation models of cubic and tetragonal $PbTiO_3$ for the *ab initio* calculations as well as the potential optimization. The solid arrows indicate atomic displacements from the ideal lattice site. The dashed arrow $\boldsymbol{P}$ represents the polarization direction.

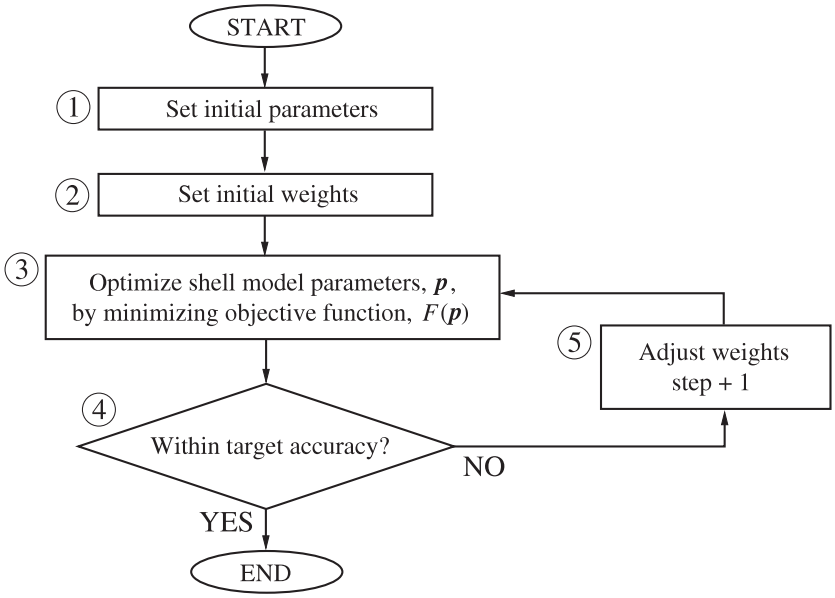

Figure 3. Flowchart explaining potential optimization procedure.

constants and elastic constants with the VASP (Vienna *Ab initio* Simulation Package) code [43, 44], which employs the plane-wave pseudopotentials based on the projector augmented wave (PAW) method [45]. The exchange–correlation energy functional is evaluated within the local density approximation (LDA) of the Ceperley–Alder form [35]. The Brillouin zone integrations are carried out with an $8 \times 8 \times 8$ Monkhorst–Pack k-point mesh [36].

The equilibrium crystal structure is calculated by relaxing the atomic configuration and the cell size using the Broyden–Fretcher–Goldfarb–Shanno (BFGS) minimization method until all the Hellmann–Feynman forces and stress components are less than 1.0×10^{-3} eV Å^{-1} and 1.0×10^{-3} GPa, respectively.

The relationship between stress σ_i ($i = 1, \ldots, 6$) and strain ε_j ($j = 1, \ldots, 6$) in the elastic region is given by,

$$\sigma_i = c_{ij}\varepsilon_j, \tag{6}$$

where the subscripts follow the Voigt notation. The six independent elastic constants in the tetragonal phase, c_{11}, c_{12}, c_{13}, c_{33}, c_{44} and c_{66}, are evaluated from the inclination of the corresponding stress–strain curve in the small-strain region ($\varepsilon_j \leqslant 0.005$). At each strain, the internal atomic coordinates are fully relaxed.

The Born effective charges and force constant matrix on a Γ-centered $4 \times 4 \times 4$ q-point mesh in the Brillouin zone are computed within a variational formulation [37] of the density functional perturbation theory (DFPT) [38, 39]. Then, the phonon dispersion relations are calculated according to the interpolation scheme described in [40, 41] from the force constant matrix on the selected $4 \times 4 \times 4$ q-points.

2.3. Potential optimization procedure

For the optimization of the shell model parameters, $\boldsymbol{p}$, we define the objective function as the following square sum of error,

$$F(\boldsymbol{p}) = \sum_i w_i \left(\frac{f_i^{\text{model}}(\boldsymbol{p}) - f_i^{\text{target}}}{f_i^{\text{target}}} \right)^2, \tag{7}$$

where f_i^{target}, $f_i^{\text{model}}(\boldsymbol{p})$ and w_i denote the *ab initio* result of a target property i, the corresponding magnitude obtained from the shell model potential and the weight, respectively.

Figure 3 shows the flowchart explaining the potential optimization procedure. First, we set the initial magnitude

Table 1. Initial weights and target accuracy for each property.

Target property	Initial weight	Target accuracy
Lattice constant	1000	±1%
Normalized atomic coordinate	500	±0.015
Elastic constant	1	±30%
Born effective charge	1	±30%
Phonon frequency (∼100 cm^{-1})	100	±10 cm^{-1}
Phonon frequency (100–500 cm^{-1})	10	±75 cm^{-1}
Phonon frequency (∼500 cm^{-1})	1	±150 cm^{-1}
Energy difference	10	±0.005 eV

of the parameters (①). Next, the initial weights are assigned according to the relative importance and magnitude of the target property (②). The weights used in this study are listed in table 1. The parameters, $\boldsymbol{p}$, are then optimized by minimizing the objective function, $F(\boldsymbol{p})$, using the Newton–Raphson method implemented in the GULP (General Utility Lattice Program) code [46] until the change in $F(\boldsymbol{p})$ between the current and previous steps is less than 1.0×10^{-5} (③). Here, the gradient of $F(\boldsymbol{p})$ is calculated by the numerical differentiation because $F(\boldsymbol{p})$ cannot be described as a simple function of the parameters. $f_i^{\mathrm{model}}(\boldsymbol{p})$ is always evaluated for stable configuration after relaxation of the cubic and tetragonal atomic structures at each minimization step. Since the Newton–Raphson minimization often brings a local minimum in the parametric space, significant errors remain in several properties at the end of the optimization in such a case. To avoid this, the weight is simultaneously adjusted. After the procedure ③, we check whether the error in each property is inside or outside the target accuracy, e_{target}, listed in table 1 (④). If the potential does not satisfy the accuracy, the current weight, w_i^{step}, of the property i that is outside the target accuracy is updated according to the following equation,

$$w_i^{\mathrm{step}+1} = \bar{e}_i w_i^{\mathrm{step}}, \qquad \bar{e}_i = \left(\frac{f_i^{\mathrm{model}}(\boldsymbol{p}) - f_i^{\mathrm{target}}}{f_i^{\mathrm{target}}} \right) \Big/ e_{\mathrm{target}} \tag{8}$$

where $\bar{e}_i$ denotes the error normalized by the target accuracy (⑤). Then, the optimization is carried out again with the new weight, $w_i^{\mathrm{step}+1}$ (③). The process ③–④–⑤ is repeated until all the errors are within the target accuracy, or no further improvement can be found.

3. Potential optimization results

Figure 4 represents the change in the sum of the errors normalized by the target accuracy during the optimization process. Here, only the errors outside their target accuracy are summed. The sum of the normalized errors at the step 0 is evaluated from the initial parameters. It drops dramatically in the first cycle, indicating that the initial parameters are successfully improved. During subsequent steps, where the weights are adjusted, the errors gradually decrease. As the errors almost converge after 12 cycles, the optimization is terminated at the 16th cycle.

Table 2 shows the optimized potential parameters for $PbTiO_3$ obtained at the 16th cycle. The target properties

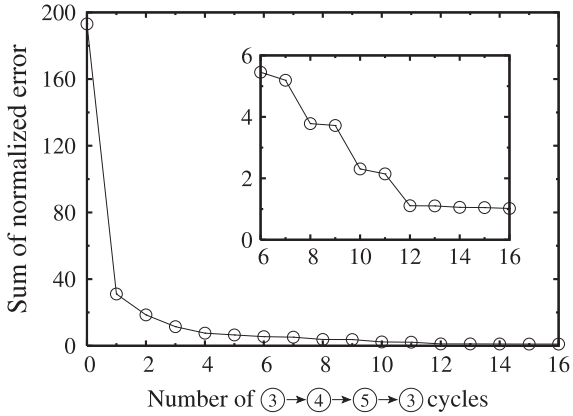

Figure 4. Change in the sum of errors normalized by the target accuracy during the optimization process for $PbTiO_3$.

Table 2. Optimized potential parameters in shell model functions for $PbTiO_3$. The radii in the cut-off function, $f_c(r)$, are $R_{c1} = 6.0$ Å and $R_{c2} = 8.0$ Å for all the short-range interactions.

Interactions	A (eV)	ρ (Å)	C (eV Å^6)	
Pb–O	2538.4110	0.300 698	2.61676	
O–O	1698.6653	0.271 756	61.84354	
Ti–O	2555.2075	0.278 391	2.25557	
Pb–Ti	387.7316	0.394 957	223.24409	
Species	X (e)	Y (e)	k_2 (eV Å^{-2})	k_4 (eV Å^{-4})
Pb	+5.495 86	−3.633 22	154.8713	22 416.67
O	+2.548 43	−4.199 17	180.9134	6 945.78
Ti	+19.369 01	−16.279 52	8829.4096	1928 581.70

derived from the optimized shell model potential and *ab initio* calculations, and their error are listed in table 3, except the phonon dispersion relations shown later. The optimized potential correctly reproduces both the cubic and tetragonal equilibrium structures. In particular, a large tetragonality in c_T/a_T and the energy difference between the cubic and tetragonal phases $\Delta E_{\mathrm{cubic-tetra}}$, which are the characteristics in $PbTiO_3$, are well reproduced. Our potential gives more accurate equilibrium structures than that of a currently available shell model potential for $PbTiO_3$, which yields $a = 3.86$ Å and $c/a = 1.031$ [30]. However, our result still slightly underestimates the experimental lattice parameter, $a = 3.90$ Å and $c/a = 1.065$ [47]. The main source of this slight error is not the shell model itself, but the well-known problem of the LDA functional in DFT calculations which is likely to underestimate the equilibrium lattice parameters of solids. In a recent publication, a new generalized gradient approximation (GGA) functional is proposed by Wu and Cohen (WC) [48]. The WC-GGA functional successfully describes the lattice parameters of both $PbTiO_3$ and $BaTiO_3$. Thus, further improvements will be expected when the shell model potential is constructed from first-principles calculations on the basis of the WC-GGA functional.

The spontaneous polarization of the optimized shell model potential is evaluated to be $P = 66.8$ μC cm^{-2} according to (1). Compared with $P = 79.8$ μC cm^{-2} obtained

Table 3. Comparison of physical properties of $PbTiO_3$ obtained from the optimized shell model and *ab initio* calculations. Only the diagonal component is shown for the Born effective charge tensors. The subscripts $\perp$ and $\parallel$ refer to directions perpendicular and parallel to the Ti–O bond, respectively. u_z indicates the internal atomic coordinate in the z direction, normalized by the lattice parameter c_T. The symbols O1 and O2 correspond to the oxygen atoms depicted in figure 2.

	Shell model	*Ab initio*	Error
Cubic phase			
a_C (Å)	3.886	3.893	0.16%
Z^*_{Pb} (e)	+2.86	+3.89	26.58%
Z^*_{Ti} (e)	+5.12	+7.22	29.13%
$Z^*_{O_\perp}$ (e)	−1.79	−2.60	31.36%
$Z^*_{O_\parallel}$ (e)	−4.41	−5.89	25.21%
Tetragonal phase			
a_T (Å)	3.854	3.867	0.34%
c_T (Å)	4.064	4.042	0.55%
c_T/a_T	1.054	1.045	0.86%
P (μC cm^{-2})	66.8	79.8	16.29%
u_z (Pb)	0.000	0.000	0.000
u_z (Ti)	0.530	0.534	0.004
u_z (O1)	0.091	0.090	0.001
u_z (O2)	0.618	0.606	0.012
c_{11} (GPa)	297.2	284.3	4.57%
c_{12} (GPa)	114.3	114.6	0.25%
c_{13} (GPa)	83.2	91.6	9.12%
c_{33} (GPa)	99.7	98.7	1.04%
c_{44} (GPa)	48.0	61.0	21.27%
c_{66} (GPa)	115.8	103.1	12.41%
$\Delta E_{cubic-tetra}$ (eV)	0.0571	0.0566	0.0005

from the *ab initio* calculations based on the Berry phase theory [49], the shell model potential underestimates the spontaneous polarization. In fact, the related property of the Born effective charge tensors defined as the coefficient of change in spontaneous polarization with respect to the sublattice displacement,

$$Z^*_{\kappa,\alpha\beta} = \frac{\partial P_\beta}{\partial \xi_{\kappa,\alpha}}, \tag{9}$$

are underestimated, as well. This deviation presumably arises from the relatively relaxed target accuracy constraints imposed during the optimization. Nevertheless, the potential qualitatively describes the important features in the perovskite oxides well, namely the strong anisotropy of the oxygen in $Z^*_{O_\perp}$ and $Z^*_{O_\parallel}$, and the anomalous enhancement in Z^*_{Ti} and $Z^*_{O_\parallel}$ compared with their nominal static charges of +4 and −2, respectively. These originate from the hybridization between the Ti 3d and O 2p orbitals [50], suggesting that the shell model potential developed properly includes the hybridization effect.

As for the mechanical properties, the elastic constants show satisfactory agreement with those of *ab initio* calculations. Structural stability, which is strongly linked with the phonon dispersion relations [51], is an important issue for dynamic simulation. Figure 5 compares the phonon dispersion curves obtained from the optimized shell model potential and *ab initio* calculations. The phonon band structures at frequencies below 500 cm^{-1} are well reproduced in both the cubic and tetragonal phases, though only the phonons at the high symmetrical points in the Brillouin zone are targeted in the optimization. Our shell model potential correctly reproduces the unstable 'soft mode' in the cubic phase (see figure 5(a)), which is closely related to a variety of structural phase transitions. In particular, the ferroelectric (FE) mode at the Γ-point and antiferrodistortive (AFD) mode at the R-point instabilities, coexistence or competition of which often plays a significant role in determining the phase transition sequence under high pressure [52] and surface reconstructions [16, 17], are successfully reproduced by the potential. Figure 6 plots the total energy per cubic unit cell as a function of the ferroelectric and antiferrodistortive displacements. The FE displacement of Ti is relative to Pb, and the oxygen atoms are simultaneously displaced proportionally to Ti with respect to the stable configuration. The AFD distortion is the clockwise-anticlockwise rotation angle of the TiO_6 octahedra repeated along the [001] direction, as illustrated in the figure. The shell model potential slightly underestimates the energy well depth of the FE-mode displacement, while it overestimates that of the AFD-mode rotation. On the other hand, no soft mode can be observed in the tetragonal phase, which indicates that the potential successfully yields the stable tetragonal structure. This was not achieved in previous studies aiming to develop a shell model potential for $PbTiO_3$ [53–55], where the phonon frequency in the tetragonal phase is not explicitly included in the potential optimization.

4. Applicability of developed shell model potential

4.1. Ferroelectric and mechanical behavior under uniaxial tension and compression

As the ferroelectricity is sensitive to the strain due to variation of the tetragonality, c/a, we set out to elucidate the applicability of the potential on the ferroelectric and mechanical behavior under uniaxial tension/compression along [001]. The uniaxial strain is applied stepwise with a small increment up to $\varepsilon_{zz} = 0.10$ in tension and up to $\varepsilon_{zz} = -0.10$ in compression. At each strain, the atomic structure is fully relaxed under the free transverse-stress condition, $\sigma_{xx} = \sigma_{yy} = 0$, by changing the x and y cell dimensions by trial and error. Note that the tetragonal symmetry (space group $P4mm$) is kept fixed during the simulations for simplicity. Thus, spontaneous polarization is always aligned to the z-axis. For comparison, *ab initio* tensile and compressive simulations are conducted in the same manner using the VASP code [43, 44] based on the PAW method [45] within the LDA [35].

Figure 7 plots the changes in polarization and stress of the tetragonal $PbTiO_3$ single crystal under the uniaxial deformation. The potential apparently underestimates spontaneous polarization. The shell model potential, however, qualitatively follows the *ab initio* results. The critical strain for ferroelectricity by the shell model, $\varepsilon^c_{zz} = -0.08$, is close to that by the *ab initio* simulation, $\varepsilon^c_{zz} = -0.09$. The stress–strain curve shows significant agreement with each other. Even at the high strain of $\varepsilon_{zz} = -0.10$, the difference in the stress is less than 10%.

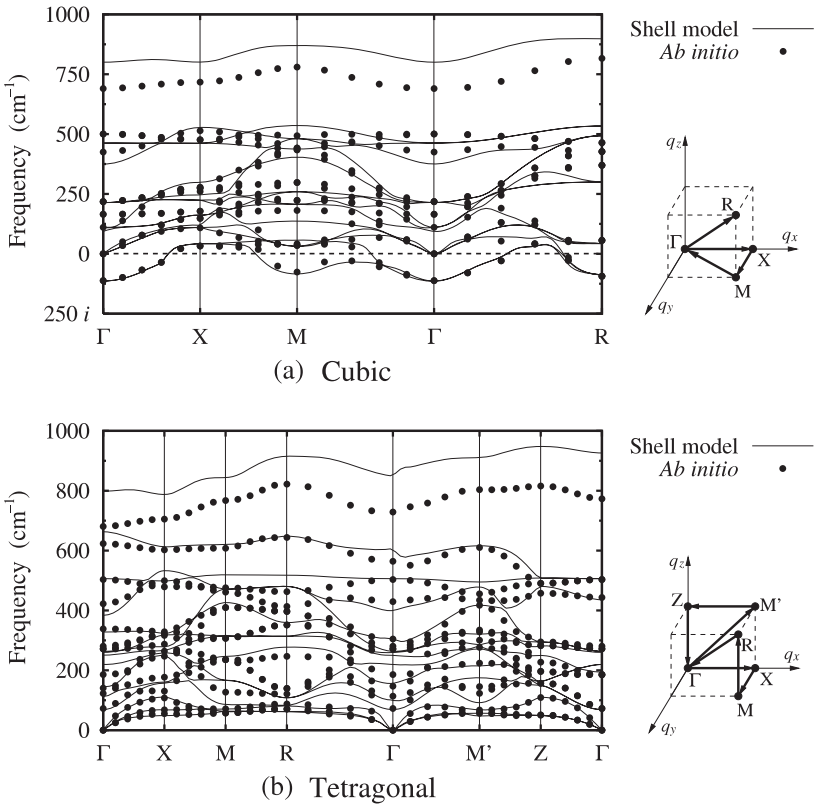

Figure 5. Phonon dispersion curves of (a) cubic and (b) tetragonal $PbTiO_3$ obtained by the optimized shell model potential (solid lines) and *ab initio* calculations (full circles). The vectors in the figure on the right represent the q-path in the Brillouin zone.

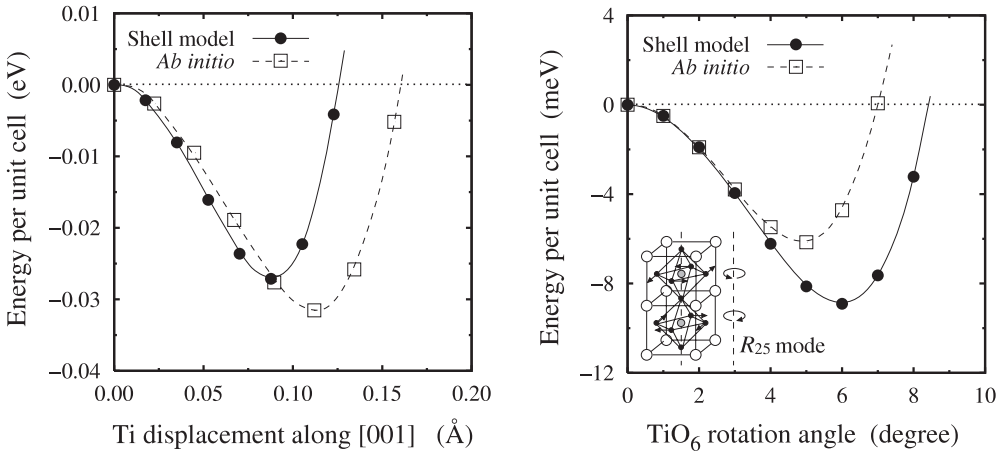

Figure 6. Comparison of total energy per unit cell as a function of the ferroelectric-mode displacement along the [001] direction (left panel) and the antiferrodistortive-mode rotation of the TiO_6 octahedra (right panel) in the cubic phase. The Ti displacement is relative to Pb.

4.2. Application to surfaces

In general, the rapid change in coordination number at a surface significantly affects the delicate balance between the long-range Coulomb and short-range repulsive interactions, which is essential for ferroelectric (FE) and antiferrodistortive (AFD) instabilities in $PbTiO_3$. A PbO-terminated (001) surface is suitable for verifying applicability of the potential because the FE and AFD distortions coexist at the surface involving c(2 × 2) surface reconstruction [16].

Figure 8 shows the simulation models for $PbTiO_3$(001) surface with the PbO-termination. Models with both (1 × 1) and c(2 × 2) surface periodicity are employed for the study of the FE phase, and AFD and FE with coexisting AFD (FE + AFD) phases, respectively. Each simulation cell contains nine atomic layers of alternating PbO and TiO_2 planes. Since the boundary is periodic, the slab is separated from those in the imaginary cell by a vacuum region with a sufficiently large thickness of 12 Å to avoid undesirable interaction between the slabs. The

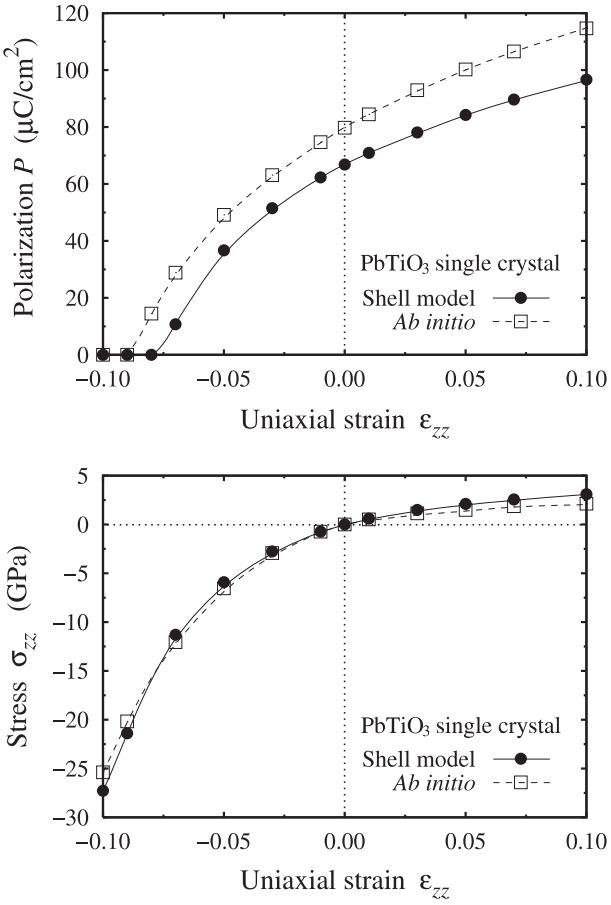

Figure 7. Ferroelectric (top panel) and mechanical (bottom panel) responses of the tetragonal $PbTiO_3$ single crystal under uniaxial deformation along the [001] direction, ε_{zz}, obtained from the optimized shell model and *ab initio* calculations.

in-plane square lattice parameter is fixed at $a = 3.891$ Å. To obtain the FE, AFD, and FE + AFD configurations, atomic relaxation is started from the slightly distorted configurations so that the systems possess the proper symmetry of the aimed structure.

Figure 9 depicts the relaxed atomic structures of the first two layers at the PbO-terminated surface in phases FE, AFD and FE + AFD, where the symbols ◯ and + represent the results obtained by the optimized shell model and by the *ab initio* calculations, respectively. For the FE and FE + AFD phases, the in-plane polarization lies along the [110] direction. The potential successfully reproduces FE and AFD as well as complex FE + AFD surface atomic configurations. The atomic positions in the FE and AFD phases are well matched with the ones obtained by *ab initio* simulations, while the oxygen atoms deviate slightly in the FE + AFD phase.

Table 4. Layer-by-layer ferroelectric distortion, δ_{FE}, and AFD rotation angle, θ_{AFD}, of the PbO-terminated surface in the FE, AFD, and FE + AFD phases. Averaged in-plane polarization is aligned along the [110] direction. δ_{FE} is in percentage of the lattice parameter, $a = 3.891$ Å. *Ab initio* results reported in [17] are shown in parentheses.

	Layer	FE	AFD	FE + AFD
δ_{FE}	1	11.81 (12.10)	—(—)	8.10 (10.68)
	2	4.70 (5.26)	— (—)	3.60 (4.36)
	3	9.22 (8.70)	— (—)	6.18 (6.35)
	4	4.09 (4.34)	— (—)	3.36 (4.10)
	5	7.94 (7.93)	— (—)	7.57 (7.29)
θ_{AFD}	2	— (—)	14.4° (12.3°)	13.4° (10.6°)
	4	— (—)	−5.7° (−3.2°)	−4.5° (−0.4°)

For a quantitative discussion, we introduce structural parameters representing the strength of the FE and AFD instabilities. The ferroelectric distortion, δ_{FE}, of each layer is defined as follows;

$$\delta_{FE,i} = \begin{cases} [\bar{\delta}_i(\mathrm{Pb}) - \bar{\delta}_i(\mathrm{O})], & (\mathrm{PbO\ layer}) \\ [\bar{\delta}_i(\mathrm{Ti}) - \bar{\delta}_i(\mathrm{O})], & (\mathrm{TiO_2\ layer}) \end{cases} \quad (i = x, y, z) \tag{10}$$

$$\delta_{FE} = \sqrt{\delta_{FE,x}^2 + \delta_{FE,y}^2}, \tag{11}$$

where $\bar{\delta}_i$ is the layer-averaged atomic displacement relative to the ideal lattice sites. The rotation angle of the TiO_6-octahedra, θ_{AFD}, is taken as a parameter representing the strength of the AFD instability. The layer-by-layer ferroelectric distortion δ_{FE} and antiferrodistortive rotation angle θ_{AFD} for each phase are listed in table 4. For comparison, the *ab initio* results [17] are shown as well. Because of the mirror symmetry in the

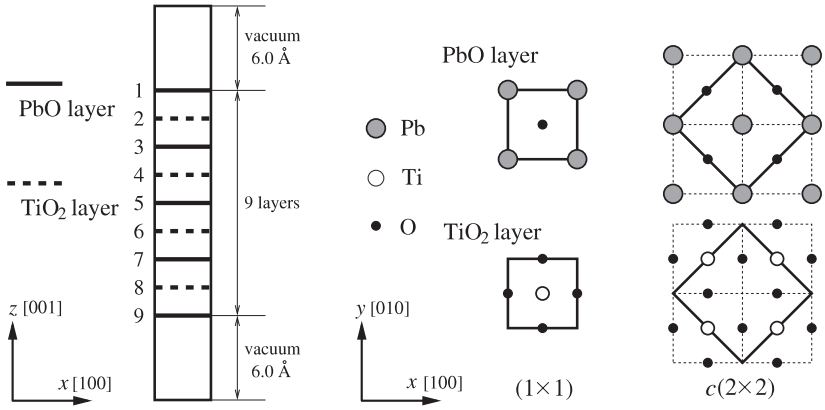

Figure 8. Simulation models for PbO-terminated (001) surface with (1 × 1) and c(2 × 2) periodicity. The solid boxes indicate the simulation cells.

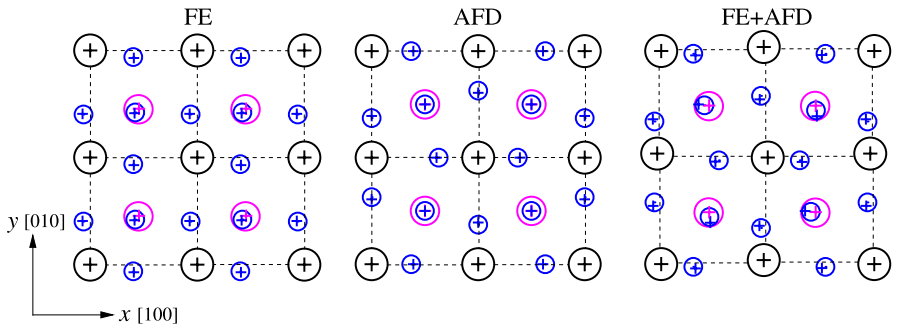

Figure 9. Relaxed atomic configurations in the FE, AFD and FE + AFD phases at the PbO-terminated (001) surface in $PbTiO_3$. Only the first two layers at the surface are depicted. The symbols ◯ and + represent the optimized shell model and *ab initio* results from [17], respectively. The large (black), medium (purple) and small (blue) symbols represent Pb, Ti and O atoms, respectively. In-plane polarization is oriented along the [110] direction for the FE and FE + AFD phases.

(This figure is in colour only in the electronic version)

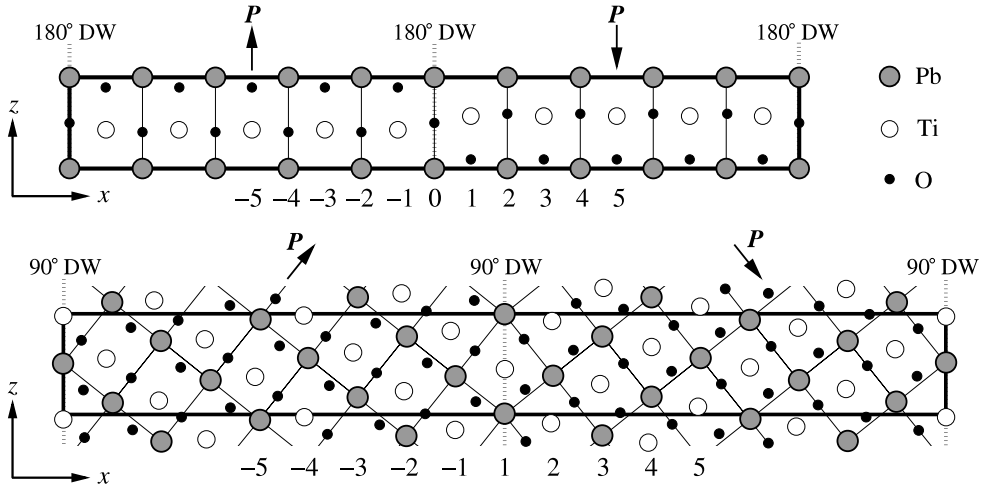

Figure 10. Simulation models for 180° and 90° domain walls containing 10 and 18 perovskite unit cells, respectively. The thick solid boxes indicate the simulation cells. The fine solid boxes in the 90° domain wall model represent a fictitious unit cell for the evaluation of local polarization (see text).

z direction, only the top half of the layers is shown. In the FE phase, δ_{FE} is in good agreement with the value obtained by *ab initio* calculations, which means that the characteristic enhancement in ferroelectricity at the PbO-terminated surface is correctly reproduced. The AFD rotation angle, which is also enhanced at the surface termination, is slightly overestimated in the AFD phase. In the FE + AFD phase, the non-zero structural parameters evidently indicate the coexistence of FE and AFD instabilities. The potential slightly underestimates the ferroelectric state while the AFD state is overestimated. Nevertheless, the deviation is small. This implies that, qualitatively, the optimized potential describes the complex surface structures well, including the c(2 × 2) reconstruction.

The shell model potential developed by Sepliarsky *et al* [30] also overestimates the AFD rotation angle, and the magnitude is close to that of our potential; $\theta^{(2)}_{AFD} = 13.8°$ for the AFD-only phase and $\theta^{(2)}_{AFD} = 13.5°$ for the FE + AFD phase [56, 57]. Moreover, they have presented the atomic displacement pattern in the FE + AFD surface with polarization along [110], which is in good agreement with our result. These suggest that our potential has comparable accuracy for surface structures with that of Sepliarsky *et al*.

4.3. Application to domain walls

Figure 10 displays the simulation models with 180° and 90° domain walls in $PbTiO_3$ containing ten and eighteen perovskite unit cells, respectively. Because of the three-dimensional periodic boundary condition, each cell has two equivalent domain walls. According to the geometrical requirement, the x, y and z cell dimensions are $10a$, a, c for the 180° domain wall model, and $18c/\sqrt{1+(c/a)^2}$, a, $a\sqrt{1+(c/a)^2}$ for the 90° model, where the tetragonal lattice parameter is $a = 3.86$ Å and $c = 4.04$ Å ($c/a = 1.046$). The distance between the domain walls in the model is large enough to avoid any undesirable influence from neighboring domain walls. To obtain stable domain wall configurations, internal atoms are fully relaxed with the cell dimensions fixed at initially set lengths.

Figure 11 represents the distribution of the ferroelectric distortion along the z axis across a 180° domain wall in

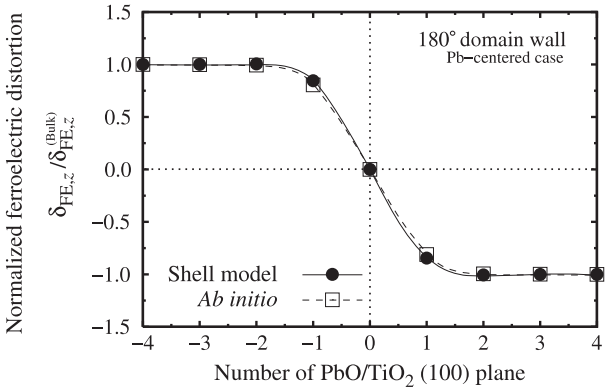

Figure 11. Distribution of the ferroelectric distortion normalized by the corresponding value of the bulk, $\delta_{FE,z}/\delta_{FE,z}^{(Bulk)}$, across a Pb-centered 180° domain wall in $PbTiO_3$. The *ab initio* calculations resulting from [18] are shown for comparison. The 180° domain wall is located at '0' of the PbO(100) plane.

$PbTiO_3$. The ferroelectric distortion is normalized by that of the bulk, $\delta_{FE,z}/\delta_{FE,z}^{(Bulk)}$. The position of the PbO or TiO_2 (100) plane in the abscissa axis corresponds to the plane number indicated in figure 10. The figure includes the results obtained by *ab initio* calculations with the same simulation model [18]. The ferroelectric distortion changes smoothly from $+z$ to $-z$ within a narrow transient region of four PbO–TiO_2(100) interplanar spacings, i.e., approximately 7.7 Å. The $\delta_{FE,z}/\delta_{FE,z}^{(Bulk)}$ distribution of the shell model potential shows excellent agreement with those of the *ab initio* result. This indicates that the potential yields the precise atomic configuration of the 180° domain wall.

In order to determine the change in the ferroelectric structure across the 90° domain wall, we adopt the measure of local polarization defined by Meyer and Vanderbilt [18]. The local polarization in the Pb-edged fictitious unit cell of the PbTiO(101) plane 'i' as depicted in figure 10, $\boldsymbol{P}'^{(i)}$, is evaluated by

$$\boldsymbol{P}'^{(i)} = \frac{e}{\Omega_c}\sum_j w_j \boldsymbol{Z}_j^* \boldsymbol{u}_j, \tag{12}$$

where Ω_c, e and $\boldsymbol{u}_j$ denote the volume of the fictitious unit cell, the electron charge and the atomic displacement vector from the ideal lattice site of atom j, respectively. Index j runs over all atoms in the cell i. $\boldsymbol{Z}_j^*$ is the Born effective charge tensor of the cubic $PbTiO_3$ bulk. In this study, we employ theoretical magnitudes of the Born effective charge tensors calculated by Zhong *et al* [51] for a fair comparison with the *ab initio* result in [20]. The weight w is set to 1/4 for Pb, 1 for Ti, and 1/2 for O, which corresponds to the number of unit cells that share the atom.

Figure 12 plots the distribution of local polarization across a 90° domain wall in $PbTiO_3$. Here, ϕ is the local polarization direction angle defined as

$$\phi = \tan^{-1}(P'_z/P'_x). \tag{13}$$

Between the '−3' and '3' planes where the 90° domain wall exists, the magnitude of the local polarization declines and the polarization direction rotates smoothly from

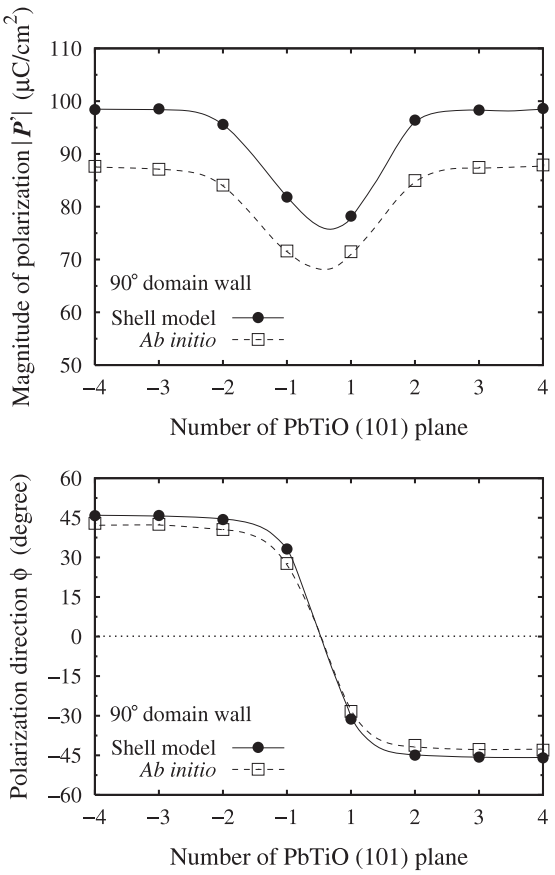

Figure 12. Distributions of magnitude of local polarization, $|\boldsymbol{P}'|$, and local polarization direction angle, ϕ, across a 90° domain wall in $PbTiO_3$ obtained from the optimized shell model and *ab initio* calculations [20]. The 90° domain wall is located between the '−1' and '1' Pb–Ti–O(101) planes.

right-up to right-down in both the shell model and *ab initio* calculations [20]. This indicates that, qualitatively, the potential describes the 90° domain wall structure well. The slight overestimation in the local polarization is attributed to the relatively large ferroelectric displacements compared to the *ab initio* results (see table 3). Note that the local polarization used here is purely evaluated from the atomic displacements, and there is no electronic contribution of core or shell charge. Thus, this does not quantitatively correspond to the 'actual' polarization evaluated by (1).

We also calculate the domain wall energy: the results are listed in table 5. The table includes the *ab initio* and experimental results as a reference. The 180° domain wall energy obtained from the optimized potential is in excellent agreement with that of *ab initio* calculations. On the other hand, the potential exhibits a slightly higher energy in the 90° case, but it is compares well with the experimental result.

The significant agreement with the *ab initio* calculations and experimental results indicate that the optimized potential has a robust capability to describe both surface and domain wall structures with satisfactory accuracy. To the best of the author's knowledge, the precise atomic structure of domain walls in $PbTiO_3$ has never been thoroughly investigated with shell model potentials. Our potential would pave the way to

Table 5. 180° and 90° domain wall energy (in mJ m^{-2}) of $PbTiO_3$ obtained from the optimized shell model potential, *ab initio* and experimental results. A stable Pb-centered case is taken for the 180° domain wall.

	Shell model	*Ab initio*	Experiment
180° domain wall	139	132[a], 150[b]	—
90° domain wall	54	35[a], 29[c]	50[d]

[a] Ultrasoft pseudopotential, LDA calculation from [18].
[b] Norm-conserving pseudopotential, LDA calculation from [19].
[c] PAW method, LDA calculation from [20].
[d] High-resolution transmission electron microscopy result from [58].

revealing complex domain wall structures, such as kinked or ledged domain walls and domain switching behaviors.

5. Conclusion

In this study, an efficient interatomic potential has been developed for $PbTiO_3$ in the framework of the shell model by fitting its parameters to reproduce properties of the single crystal derived from *ab initio* (first-principles) density functional theory (DFT) calculations. The optimized shell model potential successfully yields the equilibrium crystal structure in both the cubic and tetragonal phases. Elastic constants and phonon dispersion relations are also in good agreement with those of the *ab initio* results. In addition, both ferroelectric and antiferrodistortive instabilities, which are closely related to the structural phase transition in $PbTiO_3$, are correctly described. However, the potential tends to slightly underestimate spontaneous polarization and the related properties of the Born effective charges.

Tensile and compressive simulations along the [001] direction have revealed that the potential is capable of describing proper ferroelectric and mechanical behaviors well even under high-strain conditions. Furthermore, it has also been demonstrated that the potential successfully reproduces surface structures involving the complex c(2×2) reconstruction at the PbO-termination as well as the 180° and 90° domain wall structures in $PbTiO_3$.

The molecular dynamics simulations using our shell model potential would provide the atomic-level insight into the domain switching through the intermediate kinked or ledged domain wall structures, the domain wall kinetics in a multi-domain system, and the interaction of the domain wall and surface in a thin film. Such kinetics of domain walls or effects of temperature cannot practically be addressed by *ab initio* DFT calculations. Moreover, the comparison with the phenomenological descriptions based on the Devonshire–Ginzburg–Landau (DGL) theory [59, 60] or effective Hamiltonian [61, 62] is also an important issue for validity and reliability. These remain as future work.

Acknowledgments

This work was supported in part by a Grant-in-Aid for Scientific Research, (S) (No. 16106002), of the Japan Society of the Promotion of Science and by the Research Fellowships of the Japan Society for the Promotion of Science for Young Scientists.

References

[1] Lines M E and Glass A M 1977 *Principles and Applications of Ferroelectrics and Related Materials* (Oxford: Clarendon)
[2] Scott J F 2000 *Ferroelectric Memories* (Berlin: Springer)
[3] Ramesh R 1997 *Thin Film Ferroelectric Materials and Devices* (Boston, MA: Kluwer–Academic)
[4] Jona F and Shirane G 1993 *Ferroelectric Crystals* (New York: Dover)
[5] Cohen R E 1992 *Nature* **358** 136
[6] Wasa K, Haneda Y, Sato T, Adachi H and Setsune K 1998 *Vacuum* **51** 591
[7] Fujisawa H, Shimizu M, Niu H, Nonomura H and Honda K 2005 *Appl. Phys. Lett.* **86** 012903
[8] Gu H, Hu Y, You J, Hu Z, Yuan Y and Zhang T 2007 *J. Appl. Phys.* **101** 024319
[9] Yun W S, Urban J J, Gu Q and Park H 2002 *Nano Lett.* **2** 447
[10] Wang W Z, Varghese O K, Paulose M and Grimes C A 2004 *J. Mater. Res.* **19** 417
[11] Nonomura H, Nagata M, Fujisawa H, Shimizu M, Niu H and Honda K 2005 *Appl. Phys. Lett.* **86** 163106
[12] Chu M-W, Szafraniak I, Scholz R, Harnagea C, Hesse D, Alexe M and Gösele U 2004 *Nat. Mater.* **3** 87
[13] Hohenberg P and Kohn W 1964 *Phys. Rev.* **136** B864
[14] Kohn W and Sham L 1965 *Phys. Rev.* **140** A1133
[15] Meyer B, Padilla J and Vanderbilt D 1999 *Faraday Discuss.* **114** 395
[16] Bungaro C and Rabe K M 2005 *Phys. Rev.* B **71** 035420
[17] Umeno Y, Shimada T, Kitamura T and Elsässer C 2006 *Phys. Rev.* B **74** 174111
[18] Meyer B and Vanderbilt D 2002 *Phys. Rev.* B **65** 104111
[19] Pöykkö S and Chadi D J 1999 *Appl. Phys. Lett.* **75** 2830
[20] Shimada T, Umeno Y and Kitamura T 2008 *Phys. Rev.* B **77** 094105
[21] Hutt S, Köstlmeier S and Elsässer C 2001 *J. Phys.: Condens. Matter* **13** 3949
[22] Geng W T, Zhao Y J and Freeman A J 2000 *Phys. Rev.* B **63** 060101(R)
[23] Mo S-D, Ching W Y, Chisholm M F and Duscher G 1999 *Phys. Rev.* B **60** 2416
[24] Zhang Z, Wu P, Lu L and Shu C 2006 *Appl. Phys. Lett.* **88** 142902
[25] Geneste G, Bousquet E, Junquera J and Ghosez P 2006 *Appl. Phys. Lett.* **88** 112906
[26] Spanier J E, Kolpak A M, Urban J J, Grinberg I, Ouyang L, Yun W S, Rappe A M and Park H 2006 *Nano Lett.* **6** 735
[27] Kitagawa H, Kitamura T, Shibutani Y and Nakatani A 1997 *Molecular Dynamics for Beginners* (Tokyo: Yokendo) (in Japanese)
[28] Dick B J and Overhauser A W 1958 *Phys. Rev.* **112** 90
[29] Tinte S, Stachiotti M G, Sepliarsky M, Migoni R L and Rodriguez C O 1999 *J. Phys.: Condens. Matter* **11** 9679
[30] Sepliarsky M, Asthagiri A, Phillpot S R, Stachiotti M G and Migoni R L 2005 *Curr. Opin. Solid State Mater. Sci.* **9** 107
[31] Sepliarsky M, Stachiotti M G and Phillpot S R 2005 *Handbook of Materials Modeling* ed S Yip (New York: Springer) p 527
[32] Donnerberg H 1999 *Atomic Simulation of Electrooptic and Magnetooptic Oxide Materials* (Berlin: Springer)
[33] Khatib D, Migoni R, Kugel G E and Godefroy L 1989 *J. Phys.: Condens. Matter* **1** 9811
[34] Vanderbilt D 1990 *Phys. Rev.* B **41** 7892
[35] Ceperley D M and Alder B J 1980 *Phys. Rev. Lett.* **45** 566
[36] Monkhorst H J and Pack J D 1976 *Phys. Rev.* B **13** 5188
[37] Gonze X, Allan D C and Teter M P 1992 *Phys. Rev. Lett.* **68** 3603

[38] Baroni S, Giannozzi P and Testa A 1987 *Phys. Rev. Lett.* **58** 1861
[39] Zein N E 1984 *Sov. Phys.—Solid State* **26** 1825
[40] Giannozzi P, Gironcoli de S, Pavone P and Baroni S 1991 *Phys. Rev.* B **43** 7231
[41] Gonze X, Charlier J-C, Allan D C and Teter M P 1994 *Phys. Rev.* B **50** 13035
[42] Baroni S, Dal Corso A, Gironcoli de S and Giannozzi P http://www.pwscf.org
[43] Kresse G and Hafner J 1993 *Phys. Rev.* B **47** 558
[44] Kresse G and Furthmüller J 1996 *Phys. Rev.* B **54** 11169
[45] Blöchl P E 1994 *Phys. Rev.* B **50** 17953
[46] Gale J D 1997 *J. Chem. Soc. Faraday Trans.* **93** 629
[47] Shirane G, Pepinsky R and Frazer B C 1956 *Acta Crystallogr.* **9** 131
[48] Wu Z and Cohen R E 2006 *Phys. Rev.* B **73** 235116
[49] Resta R 2000 *J. Phys.: Condens. Matter* **12** R107
[50] Posternak M, Resta R and Baldereschi A 1994 *Phys. Rev.* B **50** 8911
[51] Born M and Huang K 1954 *Dynamical Theory of Crystal Lattices* (Oxford: Clarendon)
[52] Kornev I A, Bellaiche L, Bouvier P, Janolin P-E, Dkhil B and Kreisel J 2005 *Phys. Rev. Lett.* **95** 196804
[53] Sepliarsky M and Cohen R E 2002 *Fundamental Physics of Ferroelectrics* (*AIP Conf. Proc. No 626*) ed R E Cohen (Woodbury, NY: AIP) p 36
[54] Kitamura T, Umeno Y, Shang F, Shimada T and Wakahara K 2006 *Trans. Japan. Soc. Mech. Eng.* A **72** 817
[55] Kitamura T, Umeno Y, Shang F, Shimada T and Wakahara K 2007 *J. Solid Mech. Mater. Eng.* **1** 1423
[56] Sepliarsky M, Stachiotti M G and Migoni R L 2005 *Phys. Rev.* B **72** 014110
[57] Sepliarsky M, Stachiotti M G and Migoni R L 2006 *Ferroelectrics* **335** 3
[58] Stemmer S, Streiffer S K, Ernst F and Rühle M 1995 *Phil. Mag.* A **71** 713
[59] Devonshine A F 1949 *Phil. Mag.* A **40** 1040
[60] Devonshine A F 1951 *Phil. Mag.* A **42** 1065
[61] Zhong W, Vanderbilt D and Rabe K M 1994 *Phys. Rev. Lett.* **73** 1861
[62] Zhong W, Vanderbilt D and Rabe K M 1994 *Phys. Rev.* B **52** 6301